
Article:
Zhu, Z. and Majewski, C. orcid.org/0000-0003-3324-3511 (2020) Understanding pore formation and the effect on mechanical properties of high speed sintered polyamide-12 parts: A focus on energy input. Materials & Design, 194. 108937. ISSN 0264-1275

https://doi.org/10.1016/j.matdes.2020.108937

Materials and Design 194 (2020) 108937

Contents lists available at ScienceDirect

Materials and Design

journal homepage: www.elsevier.com/locate/matdes

Understanding pore formation and the effect on mechanical properties of High Speed Sintered polyamide-12 parts: A focus on energy input

Zicheng Zhu *, Candice Majewski

EPSRC MAPP Future Manufacturing Hub, The University of Sheffield, Sheffield, United Kingdom

HIGHLIGHTS

- The effect of energy input on pore formation, porosity and resulting mechanical properties of High Speed Sintered parts was investigated.
- Porosity, pore morphology, volume, number density and spatial distribution were examined using the X-ray Computed Tomography technique.
- A strong correlation between energy input, porosity and mechanical properties was found.
- Increasing energy input led to reduced porosity and improved mechanical properties, with pores that tended to be more spherical and distributed in sub-surface regions.
- Decreasing energy input resulted increased porosity, causing large inter- and cross-layer pores to form, which were detrimental to mechanical properties.

GRAPHICAL ABSTRACT

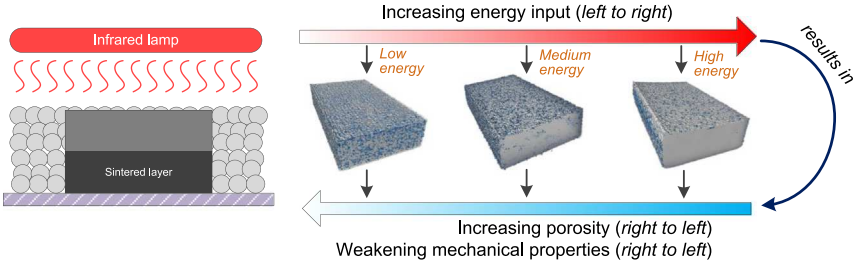

ARTICLE INFO

Article history:
Received 21 May 2020
Received in revised form 30 June 2020
Accepted 30 June 2020
Available online 08 July 2020

Keywords:
High speed sintering
Additive manufacturing
Porosity
X-ray computed tomography
Powder bed fusion
And Polyamide-12

ABSTRACT

High Speed Sintering is a novel powder-bed fusion Additive Manufacturing technique that uses an infrared lamp to provide intensive thermal energy to sinter polymer powders. The amount of thermal energy is critical to particle coalescence related defects such as porosity. This study investigates the effect of energy input on porosity and the resulting mechanical properties of polyamide-12 parts. Samples were produced at different lamp speeds, generating varying amount of energy input from a low to a high level. They were then scanned using X-ray Computed Tomography technique, following which they were subject to tensile testing. A strong correlation between energy input, porosity and mechanical properties was found, whereby pore formation was fundamentally caused by insufficient energy input. A greater amount of energy input resulted in a reduced porosity level, which in turn led to improved mechanical properties. The porosity, ultimate tensile strength and elongation achieved were 0.58%, 42.4 MPa and 10.0%, respectively, by using the standard parameters. Further increasing the energy input resulted in the lowest porosity of 0.14% and the highest ultimate tensile strength and elongation of 44.4 MPa and 13.5%, respectively. Pore morphology, volume, number density and spatial distribution were investigated, which were found to be closely linked with energy input and mechanical properties.

* Corresponding author.
E-mail address: zicheng.zhu@sheffield.ac.uk (Z. Zhu).

https://doi.org/10.1016/j.matdes.2020.108937

1. Introduction

With continued technology evolution, Additive Manufacturing (AM) is gaining increasing interests due to its capability of producing geometrically complex end-use parts in low to medium volume production [1,2]. Amongst a variety of methods in the AM family, powder bed fusion (PBF) is considered to be one of the most promising techniques in terms of part quality, accuracy and production volume and has been used in various sectors such as aerospace, automotive, medical devices and consumer goods [3–5]. High Speed Sintering (HSS) is an advanced powder bed fusion polymer AM technique specifically aimed at medium to high volume production [6].

However, one of the major defects that is usually found in PBF additively manufactured parts is the presence of internal pores which are detrimental to mechanical properties [7,8]. Advancements in micro X-ray Computed Tomography (XCT) have made it possible to assess part quality at a micro-level through observations of porosity three-dimensionally [9]. The majority of research focuses on understanding porosity variation in relation to energy density. Rouholamin and Hopkinson [10] studied the porosity of HSS parts produced using different lamp powers. The power range of 1 to 1.2 kW was found to be able to effectively reduce porosity. Dewulf et al. [11] investigated the influence of laser power, hatch spacing and scan speed on the size and distribution of pores in Laser Sintering (LS). The hatching spacing was identified as the most influential parameter that resulted in the reduced porosity level. Stichel et al. [12] explored the effect of build orientation on porosity and pore distribution of Laser Sintered polyamide-12 (PA12) parts. It was found that pore number density was a superior indicator than pore volume fraction for mechanical properties. Stoia et al. [13] identified a linear trend showing that a higher energy density led to a higher sample density in LS of PA12. Liebrich et al. [14] investigated the porosity characteristics within the thin sheets produced by LS using different build orientations and thicknesses of the thin sheets. Ituarte et al. [15] optimised the laser power and scanning speed to obtain a low porosity (8.46%) in sintering polypropylene parts. Pavan et al. [16,17] further examined the porosity, dimensional accuracy and mechanical performance of LS parts built by using different inter-layer times and energy densities. Dupin et al. [18] sought to understand pore formation mechanism and discovered that the particle size distribution and the crystallisation temperature of PA12 powders contributed to pore formation. O'Connor et al. [19] examined the porosities of PA12 and glass bead filled PA12 parts produced by HP's Multi Jet Fusion (MJF) technique. Both parts were found to be lower than 1% porosity, but the PA12 part exhibited a significantly higher Ultimate Tensile Strength (UTS) and Elongation at Break (EAB). Craft et al. [20] compared the porosity of PA12 samples produced by LS, MJF and large area projection sintering processes, and a general trend observed was that samples with a lower porosity exhibited a higher EAB.

In addition to the research on PBF polymer AM, there has been a strong interest in charactering porosity of parts produced by other AM processes in recent years [7,9]. Asberg et al. [21] reported that porosity near the edges of the sample was significantly higher than other regions within the Selective Laser Melted (SLM) sample, and the vast majority of the pores can be eliminated by applying Hot Isostatic Pressing. However, Tammas-Williams et al. [22] pointed out that gas pores would reappear during high temperature treatments. An effective method to reduce porosity as suggested by Kumar et al. [23] was to increase laser power or reduce scan speed. Tan et al. [24] studied the pore shapes and discussed that defects were primarily due to air entrapment and incomplete fusion in Laser Metal Deposition. With respect to porosity in Fused Deposition Modelling (FDM), Wang et al. [25] revealed that using a wider extrusion width and 0° raster orientation toolpath resulted in lower porosity levels ranging from 4.51% to 5.84%. For other relevant studies, readers are suggested to refer to the papers by Martin et al. [26], Carlton et al. [27], Maskery et al. [28] and Siddique et al. [29] for SLM, Tammas-Williams et al. [30] for Electron Beam Melting and Zekavat et al. [31] for FDM.

While the porosity of AM parts has drawn significant attention in the past five years, the vast majority of the research focuses on LS, SLM and EBM. There has not been a thorough understanding on porosity in relation to energy input in HSS. As pores are generally considered as critical defects, this study seeks to understand porosity and pore formation as a

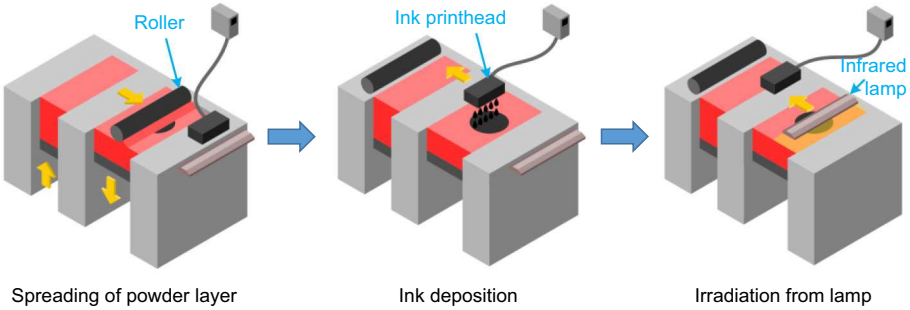

(a) Schematic of the High Speed Sintering process

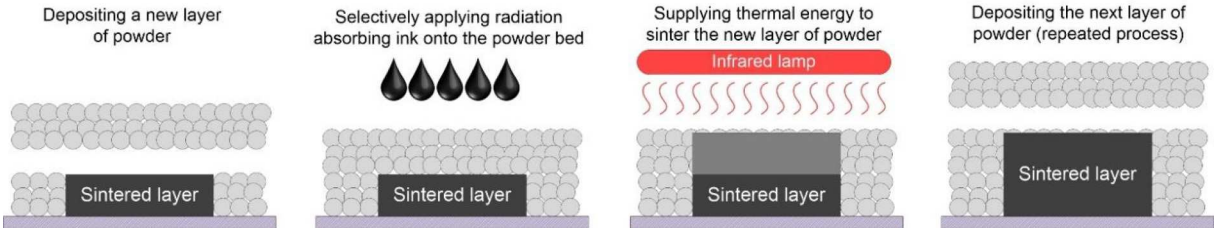

(b) Detailed view of the sintering process, adapted from [33]

Fig. 1. The High Speed Sintering process: (a) schematic of the HSS process; and (b) detailed view of the sintering process, adapted from [33].

result of varying levels of energy input in HSS, and to systematically investigate their effect on mechanical properties. XCT technique was used to examine and characterise porosity including volume fraction, pore size and morphology as well as spatial distribution. Tensile properties were measured and correlated with energy input and porosity. The experimental methods and results are presented and discussed in the proceeding sections.

2. Methods

2.1. Material

The test samples were produced using 100% virgin PA2200 powder (PA12, also known as Nylon 12, melting temperature 172–180 °C) supplied by EOS GmbH. PA12 was chosen as it is the most typical, 'standard' and repeatable material for powder bed polymer AM, and is also the most well-documented material to date for HSS. The average powder size was 56 μm and d_{90} was 90 μm.

2.2. The high speed sintering process and machine

In the High Speed Sintering process shown in Fig. 1a, a fresh layer of powder is first coated and pre-heated to a certain temperature, typically 20 °C below the melting temperature of the material. This is followed by jetting the radiation absorbing ink from the inkjet printhead onto the newly coated layer. An infrared lamp, as a thermal energy source, passes over the entire powder bed. The heat causes the ink to rapidly absorb thermal energy, leading to the sintering and consolidation of underlying powder particles [32]. Areas that are not covered by the ink remain unsintered, as depicted in Fig. 1b. A new layer of powder is applied, and the process continues until the object is built. In this study, a small Voxeljet VX200 HSS system with a maximum build size of $300 \times 200 \times 150$ mm^3 was used to manufacture the test samples.

2.3. Thermal energy input and lamp speed

Energy input has been widely considered to be one of the most critical factors that determines the microstructure and mechanical properties of parts fabricated by PBF processes [34,35]. The energy input from the lamp per unit area (E, J/mm^2) as a function of lamp speed is expressed in Eq. (1), where P is the lamp power (W), v is the lamp speed (mm/s), and L is the heated length of the lamp (mm).

$$E = \frac{P}{v \times L} \tag{1}$$

The lamp used in this study had a heated length (L) of 300 mm, with a power of 1000 W. Therefore, the energy variations have been assessed through the use of varying values of lamp speed. In addition, the lamp was provided by Victory Lighting [36]. The reflector was built into the lamp itself, covering 180° of the surface area. The lamp traversed at a height of 50 mm from the prepared powder bed surface, creating homogeneous heat signatures on the bed according to Victory Lighting [36].

2.4. Experimental design

Prior to the experiments documented in this paper, a series of trials had been performed to identify the HSS processing window. A lamp speed of 70 mm/s at full lamp power was identified to be the lowest speed that was valid for a successful build. If lower than 70 mm/s, excess energy will result in parts being over-sintered with the surrounding powder, causing print failure and/or powder removal issues. If using a lamp speed faster than 120 mm/s, rigid parts cannot form as a result of a significant lack of energy to enable proper consolidation of powder particles. Therefore, lamp speeds ranging from 70 to 120 mm/s were used, with an increment of 10 mm/s for each build, which resulted in six sets of builds in total.

In each set of builds, five ASTM D638 Type I tensile bars [37] and two cuboids of $8 \times 20 \times 3.2$ mm^3 (XYZ) were produced, as shown in Fig. 2a. In order to minimise any unexpected energy distribution variations from the lamp, the central area of the bed i.e. 150 mm wide in the Y-axis was used as shown in Fig. 2b (please note the width of the effective build area was 200 mm according to the build volume presented in Section 2.2). Standard procedures recommended by Voxeljet were followed. The powder bed was first preheated to 160 °C for 45 min. The printing process was conducted in air (no inerting) and the layout of the machine is shown in Fig. 2b. Upon finishing the build, the automatic cool down routine started, which included depositing additional 10 blank layers of powder to reduce the cooling rate, decreasing and maintaining the bed temperature at 60 °C for four hours, turning the heaters off and keeping the samples in the chamber for another two hours. Other process parameters used in the experiments are summarised in Table 1 below. The printed cuboids were scanned in XCT to examine porosity, and tensile bars were used for tensile testing.

2.5. X-ray computed tomography

XCT scans were performed in Nikon XT H 225 system. An accelerating voltage of 100 kV, power of 17.6 W and 500 ms exposure were used in the scans. These were recommended scan parameters by Nikon. The voxel size was 10 μm, which provided fine precision to examine pore size and distribution. 3D data was reconstructed from the 2D

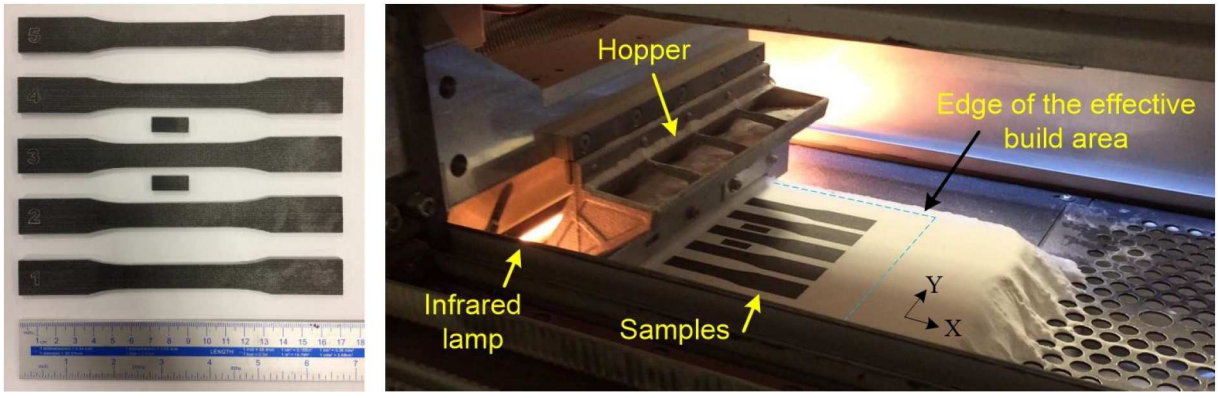

Fig. 2. High Speed Sintering: (a) printed tensile bars and cuboids; (b) samples being produced on the Voxeljet HSS system.

Table 1
HSS process parameters used in this study.

Process parameter	Value
Lamp speed	70, 80, 90, 100, 110 and 120 mm/s
Lamp power	1000 W
Ink grey level	3 (more information can be referred to [38])
Layer thickness	0.1 mm
Preheating: powder bed temperature and time	160 °C for 45 mins
Cool-down: powder bed temperature and time	60 °C for 4 h and turned off for 1 h

radiographs using a filtered back projection algorithm. The data was then analysed using FEI Avizo 9 software with segmentation by the Otsu method [39]. To reduce erroneous estimation introduced by the scan dataset noise, pores that contained a minimum of 8 voxels ($2 \times 2 \times 2$) were analysed, which was consistent with other studies reported in the literature [12,14,28]. Porosity was quantified and analysed, along with pore volume, number density, shape and spatial distribution.

2.6. Tensile testing

Tensile tests were performed on Tinius Olsen tensile machine to quantify UTS, EAB and Young's modulus of the test specimens, according to ASTM D638 Standards [37]. The test speed was 5 mm/min. The tensile load was applied perpendicular to the build direction of the samples.

2.7. Scanning electron microscopy (SEM)

The cuboids were examined in SEM as another approach for pore morphology characterisation. In addition, after the tensile testing, the fracture surfaces of the tensile specimens were also characterised in SEM to investigate pore spatial distribution. The specimens were gold coated in vacuum. The SEM was performed on a Tescan Vega3 system in 10 kV, with a maximum magnification of 3000×.

2.8. Mercury intrusion porosimetry measurements for porosity validation

In order to cross-evaluate the results of porosity measurements obtained by XCT, additional mercury intrusion porosimetry (MIP) was conducted on a Micromeritics® AutoPore V system, as shown in Fig. 3a. In each measurement, a cube was held in a section of the penetrometer cell shown in Fig. 3b. The cube was subject to low and high pressure tests in sequence, with a starting pressure of 206.8 kPa, pressure increments from 68.9 to 1.7×10^4 kPa at different stages, an ending pressure of 4.1×10^5 kPa, advancing and receding mercury contact angle of 130°, and the equilibrium time of 10s.

3. Results

3.1. Porosity and mechanical properties

The results of the porosity and the resulting mechanical properties are presented in Table 2. The porosity (%) was determined by calculating the ratio of total volume of the pores over total volume of the sample. A strong correlation between energy input, lamp speed, porosity/bulk density and mechanical properties can be identified, as demonstrated in Fig. 4. A higher energy input resulted in a higher level of density (i.e. a lower level of porosity), leading to higher UTS, EAB and Young's modulus. On the contrary, increasing the lamp speed, which effectively reduced the amount of energy input, led to a more porous structure and reduced mechanical strength.

3.2. Pore volume and density

3.2.1. Pore equivalent diameter and average pore volume

Equivalent diameter, i.e. the equivalent spherical diameter, is a factor for describing the volume of a pore or an object. It is defined as the diameter of a sphere of the same volume. Fig. 5 shows the distribution of equivalent diameter of pores for all sets of samples. It appeared that pore quantity increased significantly from set 1 to set 3. The majority of the pores is small with an equivalent diameter lower than 0.0375 mm. From sets 3 to 6, there was a steady increase in the total number of relatively larger pores (equivalent diameter > 0.1125 mm), which resulted in the increased overall porosity level. In addition, there was a noticeable increase in the number of large pores in the range from an equivalent diameter of 0.1125 mm to 0.2250 mm. This suggested that, when gradually reducing the amount of energy input, small pores started to appear, followed by the formation of large pores if the energy input continued to fall.

The average pore volume (shown in Eq. (2)) in relation to porosity and energy input is plotted in Fig. 6. It shows that porosity is closely linked with average pore volume, namely, a higher level of porosity generally indicates a larger pore in average resulting from reduced energy input (increased lamp speed).

$$\text{average pore volume} = \frac{\text{total volume of all pores}}{\text{total number of pores}} \left(\text{mm}^3\right) \tag{2}$$

3.2.2. Pore number density

The pore number density of a sample (shown in Eq. (3)) represents the number of pores that are present per cubic millimetre. Fig. 7 shows the pore number density in relation to energy input and porosity. A general trend is that pore number density rose along with the increase in porosity level from sets 1 to 5 (energy inpiut from 0.048 to 0.030 J/mm^2). However, as the porosity level further increased from 3.46% to 7.36% (energy input from 0.030 to 0.028 J/mm^2), there was a slight decrease in pore number density. It suggested that, while pores became larger in set 6, there were reduced number of pores. Please note that average pore volume and pore number density can sometimes be misleading, and further discussion on these two parameters in relation to porosity and mechanical properties will be presented in Section 4.2.2.

$$\text{pore number density} = \frac{\text{total number of pores within the sample}}{\text{volume of the sample}} \left(mm^{-3}\right) \tag{3}$$

3.3. Spatial distribution of pores

3.3.1. Pore spatial distribution across the entire sample

Pores within the cuboid samples in sets 1, 4 and 6 are rendered in Fig. 8 where the samples are in white and pores are in blue. These three sets represent the typical patterns of pore spatial distributions at different porosity levels. In set 1, the majority of the pores formed near the top and side surfaces (Fig. 8a). With an increase in the lamp speed in set 4, the amount of thermal energy input into the sample reduced, leading to pores starting to form near the bottom surface, as shown in Fig. 8b. With a further increase in the lamp speed to 120 mm/s in set 6, pores tended to form throughout the entire sample (Fig. 8c). This indicates that thermal energy is a critical factor for pore formation. In the areas where there is a lack of energy due to the fast moving infra-red lamp or temperature difference between the sintered powder and surrounding un-sintered powder, pores are more likely to form. The underlying mechanism of pore formation is discussed in Section 4.1.

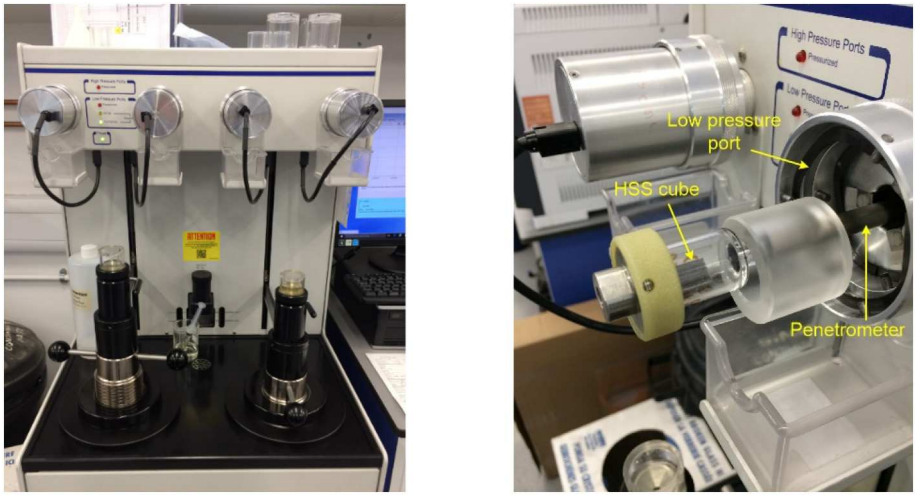

Fig. 3. Mercury intrusion porosimetry: (a) the Micromeritics® AutoPore V system and (b) placing an HSS sample into the low pressure chamber.

Table 2
Porosity, mechanical properties and XCT tomography images. The images show the front view of a projection slice of the sample, and the build direction is from bottom to top.

Set number	Lamp speed (mm/s)	Energy input per unit area (J/mm^2)	Ultimate tensile strength (MPa)	Elongation at break	Porosity (volume fraction)	Tomography image
1	70	0.048	44.4	13.5%	0.14% (measured by XCT), 0.12% (measured by MIP)	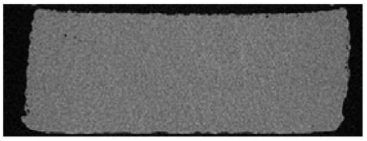
2	80	0.042	43.9	12.3%	0.20% (XCT), 0.17% (MIP)	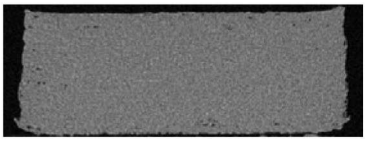
3	90	0.037	42.4	10.0%	0.58% (XCT), 0.55% (MIP)	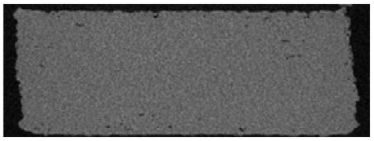
4	100	0.033	39.3	7.1%	1.49% (XCT), 1.56% (MIP)	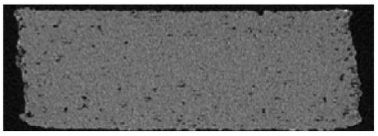
5	110	0.030	32.5	4.8%	3.46% (XCT), 3.57% (MIP)	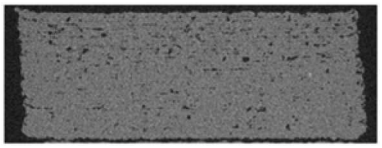
6	120	0.028	28.6	4.2%	7.36% (XCT), 7.49% (MIP)	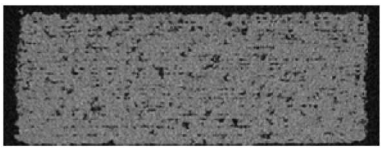

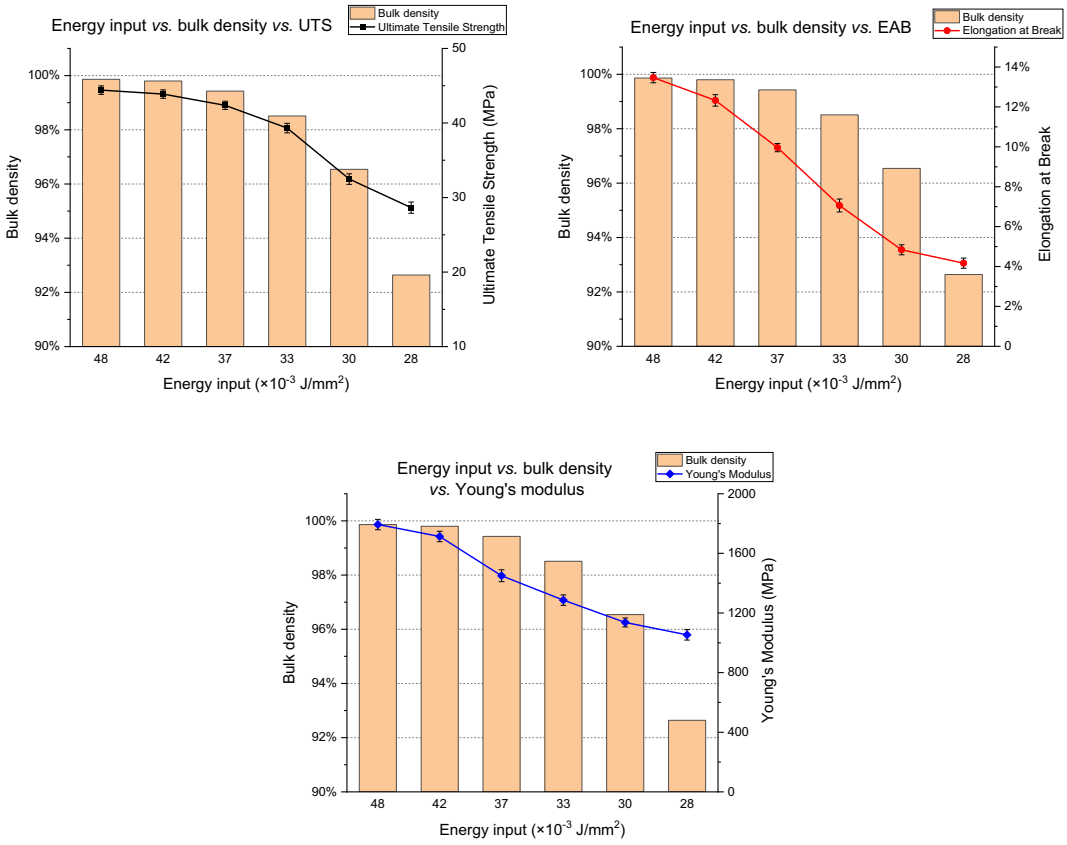

Fig. 4. Relationships between energy input, bulk density (i.e. 100% - porosity) and mechanical properties.

3.3.2. Pore spatial distribution along the build direction

The porosity variations along the build direction of the samples in sets 1–6 are plotted in Fig. 9 and are described as follows.

- Set 1 (Fig. 9a): the porosity remained in a very low level close to 0.1% along the build direction. However, the porosity started to increase rapidly in the top layers, including the top layer and the layers close to the top layer.
- Sets 2 and 3 (Fig. 9a): the trend for porosity variation is similar to set 1 except the bottom layers where there was a slight and gradual increase in porosity. The porosity then dropped back to a very low level equivalent to set 1. The fracture surface of a tensile bar in set 2 is imaged in Fig. 10, which shows the pores that formed between the bottom layers, causing the slight increase in porosity. Please note that the tensile bars were built together with the cuboid samples with the same height.
- Set 4 (Fig. 9a): the porosity level at the bottom layers of set 4 was approximately 1–2% higher than that in sets 1–3. It gradually reduced in mid-layers, which was likely due to heat accumulation within the sample as the build progressed. After the gradual reduction, the porosity then gradually re-increased as the HSS process continued towards completion.
- Set 5 and 6 (Fig. 9b): Sets 5 and 6 have a distinct pattern of porosity variations compared with sets 1–4. The porosity level increased along the build direction, indicating an increasingly incomplete fusion of powder. Readers can also refer to the XCT tomographic images shown in Table 2 where the samples in sets 5 & 6 became increasingly porous along the build direction. In addition, it was observed that there were porosity peaks that periodically appeared along the build direction shown in Fig. 9b, particularly for set 5, corresponding approximately to the layer thickness of 100 μm. This was likely related to layer thickness and the existence of inter-layer pores [11], which will be further discussed in Section 4.1.3.

3.3.3. Pore arrangement: inter-layer pores

The tomographic images, in particular sets 5 and 6 in Table 2 show that pores largely formed at areas where two adjacent layers bonded. With the lamp speed increased from sets 1 to 6, leading to reduced energy input, it is likely that there was insufficient and decreasing amount of heat at the surface that could fully penetrate through the current layer. As a result, individual powder particles would be likely to sinter less, and pores would be more likely to form. SEM micrographs in Fig. 11 have also confirmed the substantial presence of inter-layer pores. Further discussion will be given in Section 4.1.3 and Fig. 17.

3.4. Pore sphericity

Sphericity is the measure of how closely the shape of an object approaches that of a mathematically perfect sphere, which is represented by '1'. Any particle that is not spherical has sphericity less than 1. Some examples of pores are shown in Fig. 12, in which (a) and (b) are the SEM micrographs of two pores and (c) is the rendering of a pore in three-dimensional.

Fig. 13 shows the distribution of the pore sphericity in relation to pore volume for all sets of samples. In each set, pores are divided into two groups by volume, namely, pores that are larger or smaller than the average pore volume of each set, respectively. By doing so, a correlation between sphericity and volume can be identified. For large pores (≥average pore volume, blue bars), they tended to be less spherical (i.e. a lower sphericity value). Small pores, by contrast, tended to be more spherical, indicated by red bars. It was also found that the blue bars were shifting towards the sphericity value of 0.1, as the energy input continued to decrease from 0.037 to 0.028 J/mm^2 (from sets 3 to 6). This means that pore shape became less regular as the energy input decreased and pore volume increased.

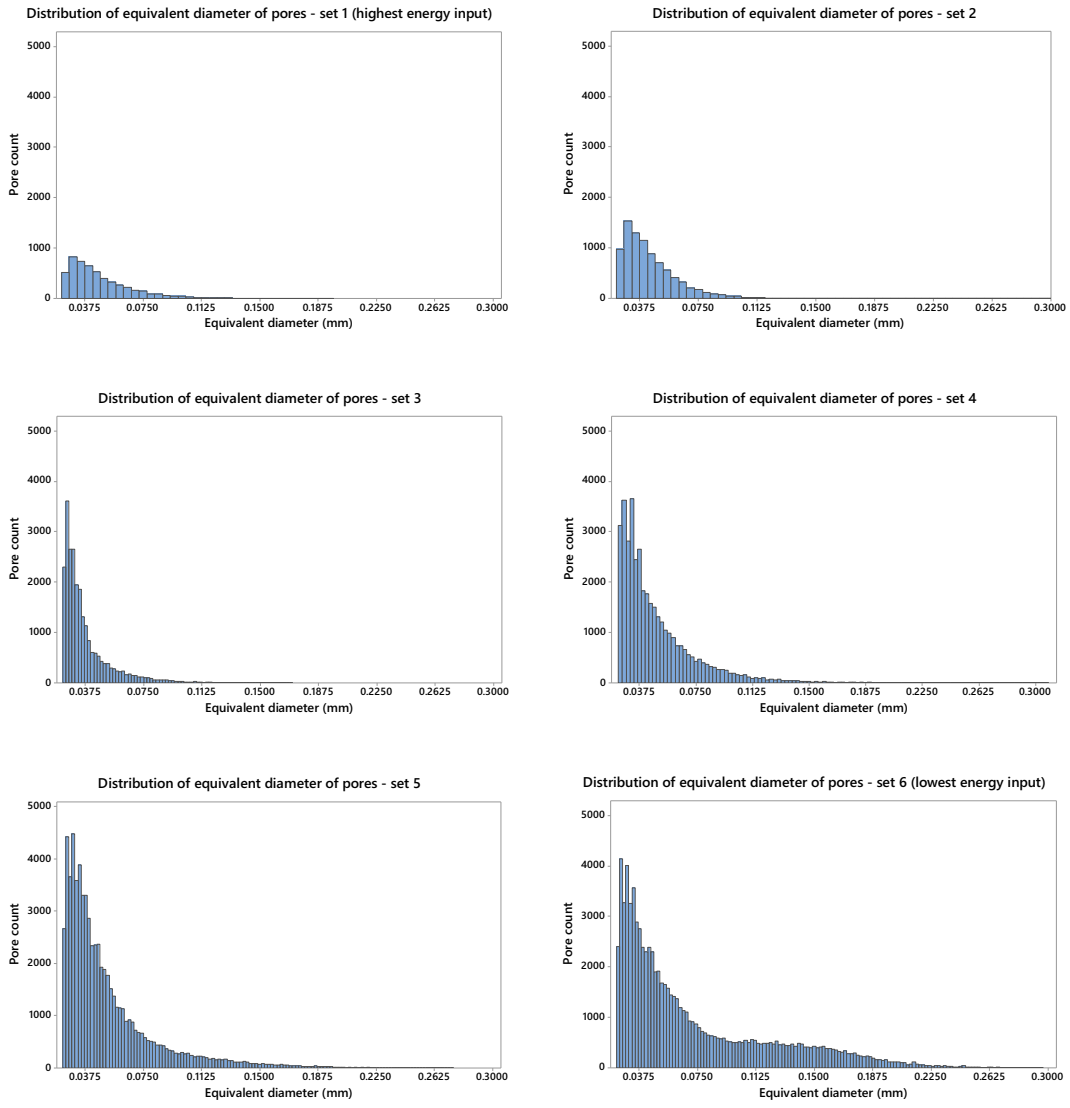

Fig. 5. Distribution of equivalent diameter of pores.

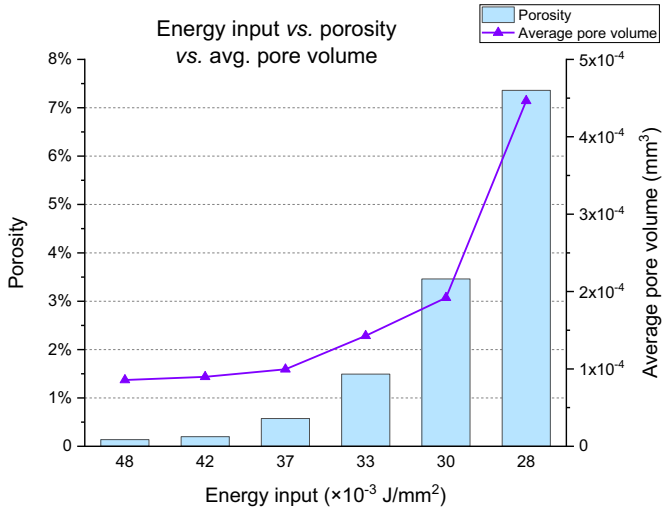

Fig. 6. Average pore volume, porosity and energy input.

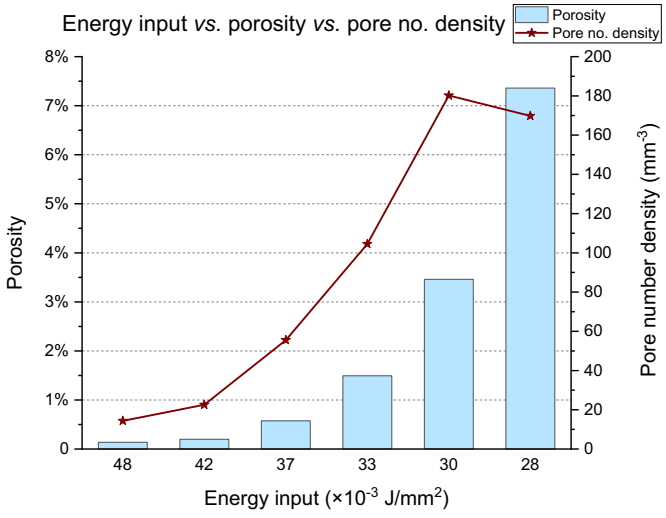

Fig. 7. Porosity and pore number density.

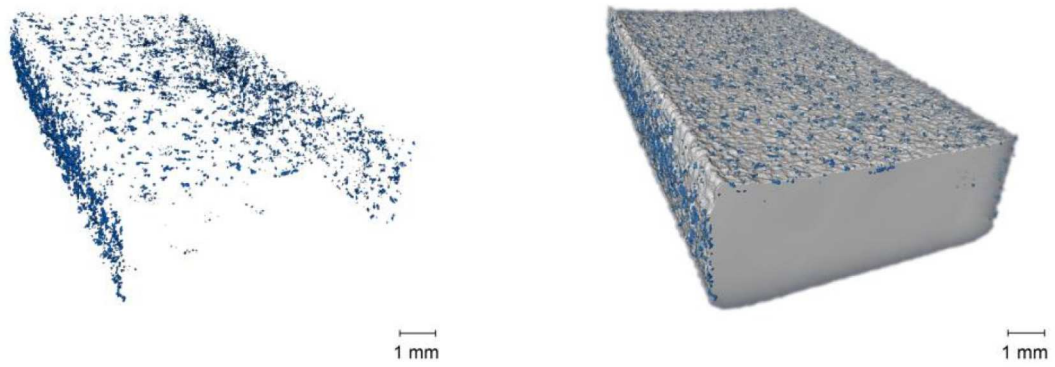

(a) Set 1, lamp speed 70 mm/s, porosity 0.14%, highest energy input

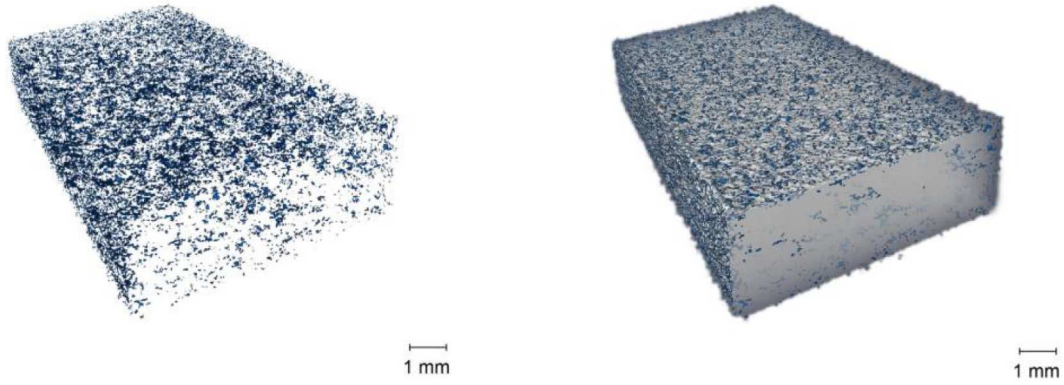

(b) Set 4, lamp speed 100 mm/s, porosity 1.49%, medium energy input

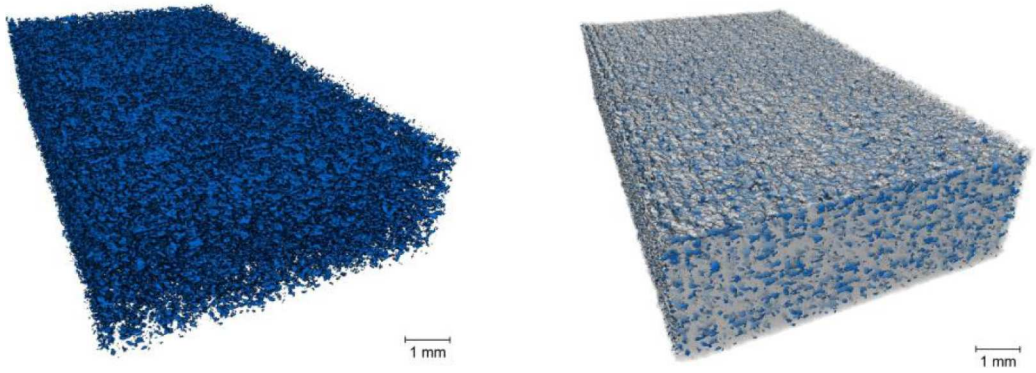

(c) Set 6, lamp speed 120 mm/s, porosity 7.36%, lowest energy input

Fig. 8. Rendering of pores within the cuboid samples in sets 1, 4 and 6, from XCT tomography data. Pores are in blue and samples are in white. (For interpretation of the references to colour in this figure legend, the reader is referred to the web version of this article.)

4. Discussion

4.1. Effect of thermal energy input on pore formation

4.1.1. Degree of fusion between powder particles

The results presented in Table 2 and Fig. 4 show that energy input, as a direct consequence of lamp speed, is fundamental to pore formation. The amount of energy input largely determines the degree of fusion between powder particles, in addition to other factors such as viscoelasticity [40,41]. Thermal energy from the lamp causes powder particles to fuse and consolidate, as illustrated in Fig. 14a. In general, the shell of the powder melts, causing the molten polymer to form necks between neighbouring particles. The difference between the average pressure on the contact area and the surface tension along the peripheries of the two adjacent particles induces a sintering force, which is the thermodynamic force that drives neck growth and shrinkage [40,42].

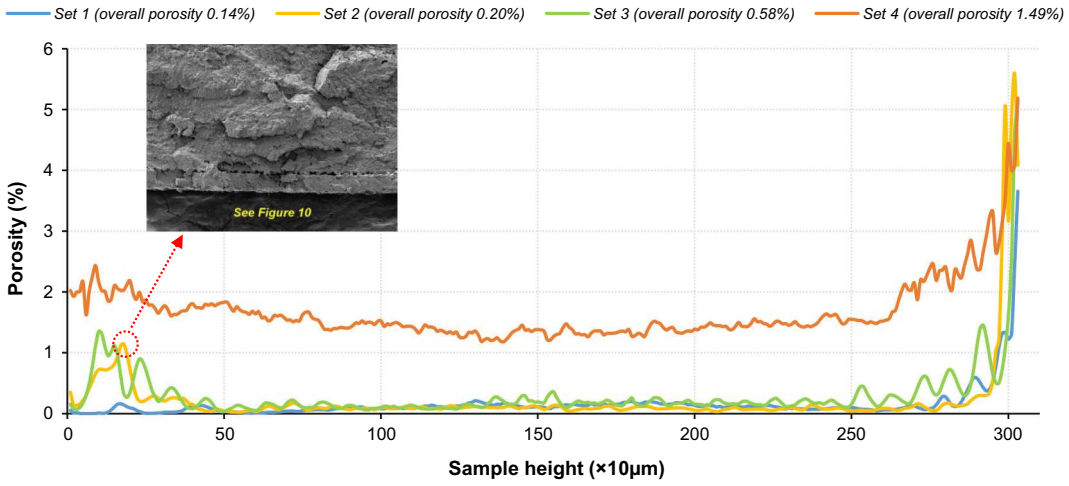

(a) Porosity along the build direction for sets 1 to 4

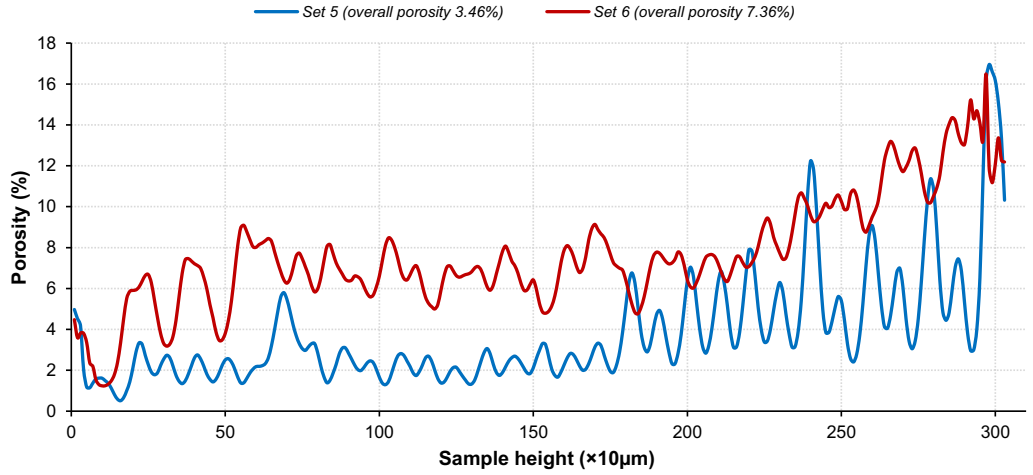

(b) Porosity along the build direction for sets 5 and 6

Fig. 9. Porosity variations along the build direction. Note that, the X-axis is the sample height [i.e. height = the X-axis reading × 10 μm], and the Y-axis is the porosity level. Also note that, in order to clearly show the porosity variations, (a) is the in the scale of 0–6% porosity in the Y-axis, and (b) is in the scale of 0–18% porosity in the Y-axis.

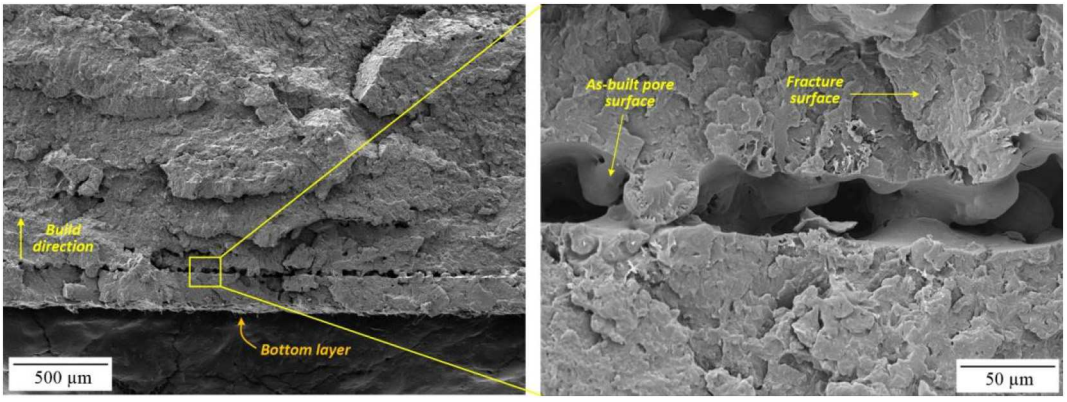

Fig. 10. SEM micrographs of the fracture surface of a tensile bar in set 2. It shows the pores near the bottom layer, causing a slight increase in porosity level shown in Fig. 9(a).

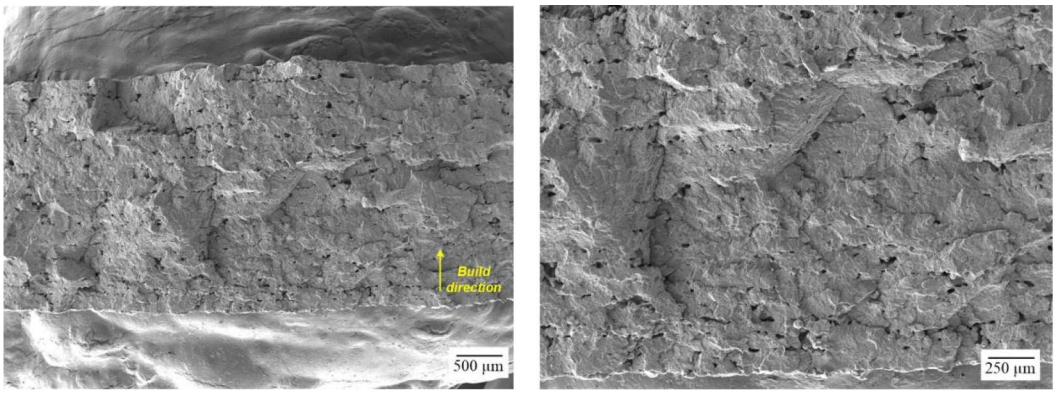

(a) Set 4, fracture surface

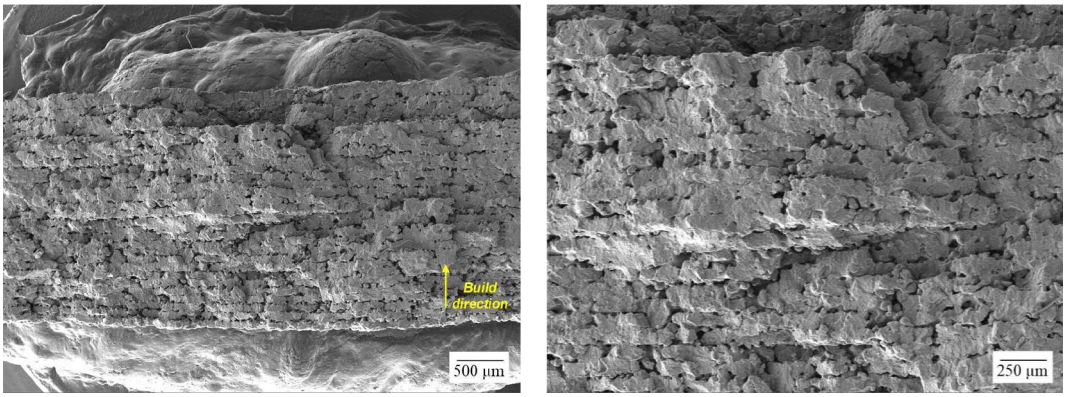

(b) Set 6, fracture surface

Fig. 11. SEM micrographs of the fracture surfaces of the tensile bars in sets 4 and 6, showing the presence of inter-layer pores.

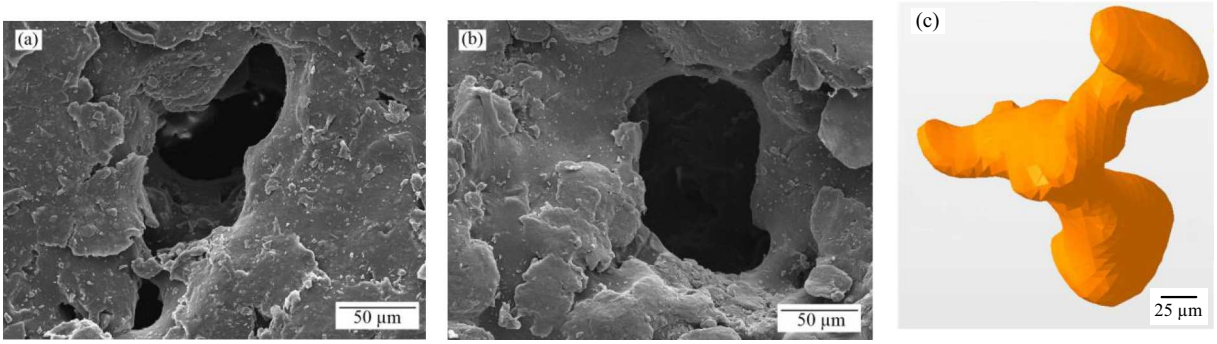

Fig. 12. Three examples of pores. (a) and (b) are the SEM images of the two pores on the specimen surfaces and (c) is the volume rendering of a pore in 3D.

However, insufficient input energy results in incomplete fusion, leaving voids between particles, as depicted in Fig. 14b. By contrast, consolidation of powder particles is promoted with a greater amount of energy input resulting from a slower lamp speed, which leads to reduced porosity.

Fig. 15 shows different degrees of powder fusion, which resulted from the highest, medium and lowest energy input when using the lowest, medium and highest lamp speeds, respectively. Comparing Fig. 15a with b and c, it was revealed that reducing energy input caused incomplete fusion. The incomplete fusion does not enable particles to fully coalesce, resulting in necking between particles within a layer and between neighbouring layers [40]. This necking phenomenon creates a space between particles as illustrated in Fig. 14b, which eventually leads to pore formation, in some cases inter- and cross-layer pores (see Section 4.1.3). Partially sintered particles and voids as a result of lack of fusion can be observed in Fig. 15b and c. Due to the lowest amount of energy input, set 6 has more unfused or partially sintered powder particles than sets 1 and 4. In addition, given that the definition of the layers can still be clearly seen in Fig. 11, it appeared that the complete powder fusion and consolidation did not occurred in sets 4 and 6.

When using a higher amount of energy input, the temperature of powders will rise. This tends to favour melting of current layer as well as re-melting of previous layers, which enhances bonding between particles and reduces porosity. This is because the elevated temperature enables large particles to be melted more completely, resulting in a lower melt viscosity [47]. A low melt viscosity is of high importance to HSS

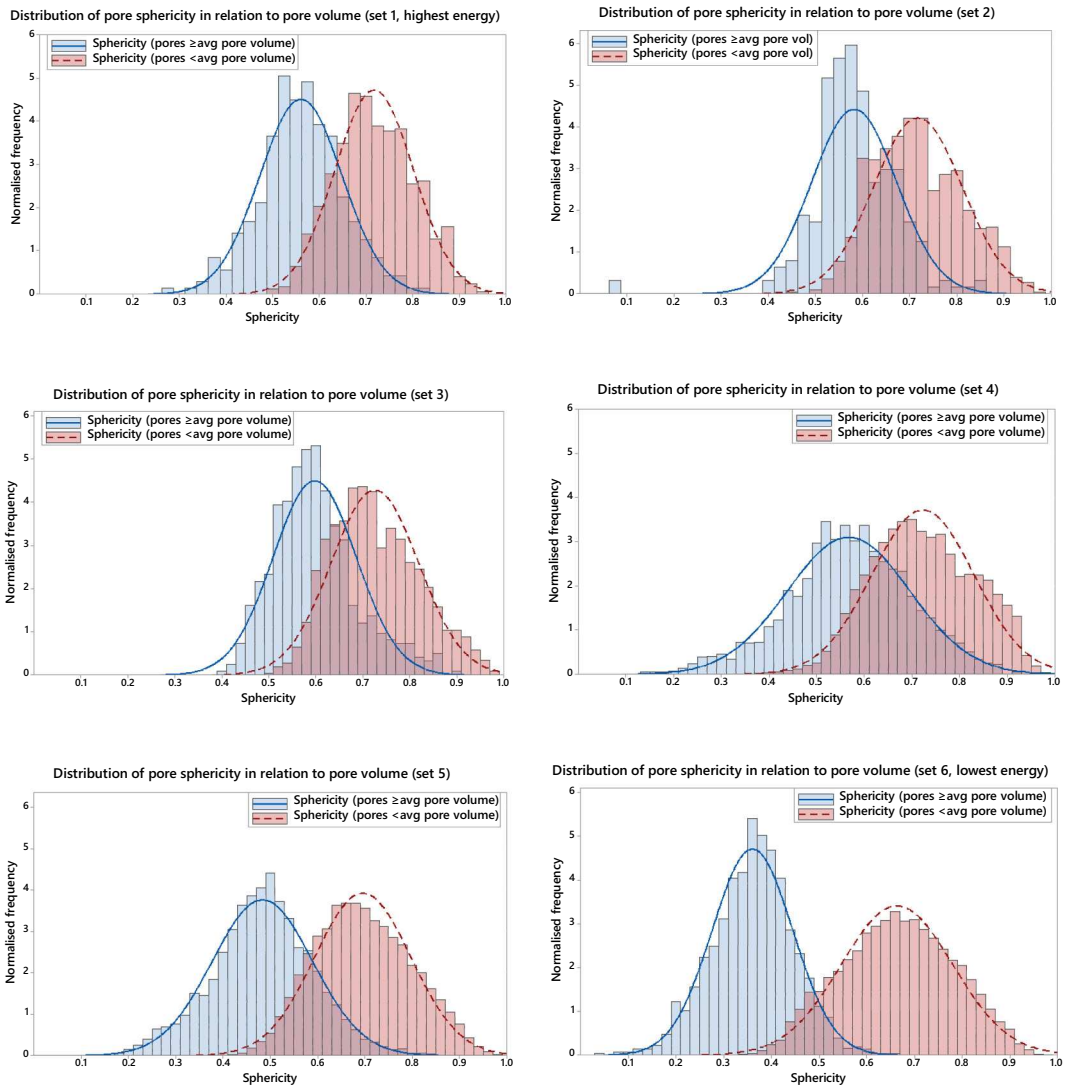

Fig. 13. Distributions of pore sphericity in relation to pore volume. Larger pores (≥ average pore volume) are less spherical (i.e. have a low sphericity value); smaller pores (< average pore volume) are more spherical (i.e. have a high spherical value).

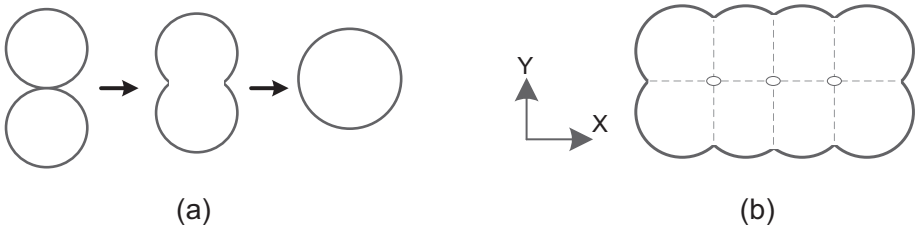

Fig. 14. Schematic representation of the sintering of particles based on the Frenkel-Eshelby model [43–45]: (a) sintering sequence for two spherical particles and (b) sintering of multiple particles, adapted from [40,46].

because there is no additional compacting force in the HSS process. Unlike injection moulding where a holding pressure is applied during part formation resulting in high density, HSS relies on melted particles themselves to flow and consolidate, as shown in Fig. 14a. The lower melt viscosity improves the flowability, which increases the tendency of melted particles to flow outwards, reducing the voids between particles and thus increasing density [48]. As the HSS process continues, the heat generated on the current layer transmits to previous layers, causing continued heat accumulation. Maintaining an elevated temperature during the course of a build allows more time for long molecular chains to rearrange and form at high temperature, and to enhance the level of bonding between subsequent layers. This ultimately results in improved tensile strength [49].

In addition, it is worth noting that other researchers reported that an excess amount of input energy could have a negative effect on porosity [46,50]. The excess heat over-melts powders and polymer pyrolysis occurs, which consequently creates a porous structure [51]. However, these thermal phenomena are generally found in laser-based processes

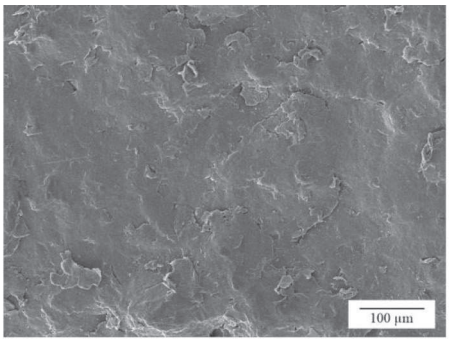

(a) Set 1, 0.048 J/mm^2 energy input

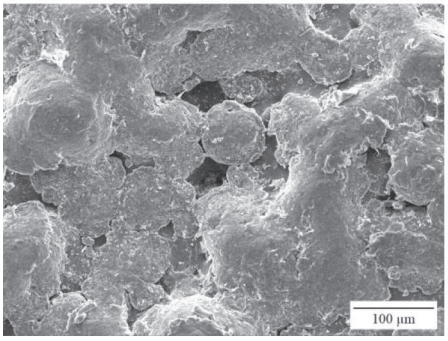

(b) Set 4, 0.033 J/mm^2 energy input

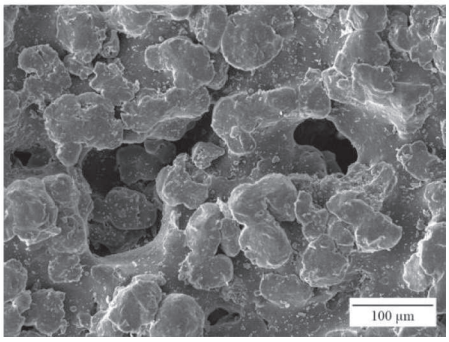

(c) Set 6, 0.028 J/mm^2 energy input

Fig. 15. Top surface of the cuboid samples showing different degrees of powder consolidation caused by the highest, medium and the lowest amount of energy input, respectively. In this figure, b and c show an incomplete powder fusion with partially sintered particles.

where a laser beam provides intensive energy and overly high energy can easily cause over-melting of powders. Whereas, in HSS, the infrared lamp is used as the energy source that irradiates the entire powder bed as it moves across, as shown in Fig. 1. While the area that is covered by ink absorbs significantly more energy supplied from the lamp, a proportion of the energy is also absorbed by the un-printed powder. Above a certain level, this leads to unwanted 'hardening' of this powder, preventing reliable part removal without damage. This restricts the possibility of further increasing energy input into the parts themselves whilst still being able to remove them successfully. The lamp speed of 70 mm/s was the lowest achievable speed (i.e. the highest achievable input energy, 0.048 J/mm^2) in this study, and the over-melting of powders and the resultant increased porosity were not observed.

4.1.2. Pore distribution

As discussed above, inadequate energy input results in a lower degree of powder fusion and consequently the temperature of powder particles is lower than a critical level, causing pores to form. Fig. 16 shows a series of XCT images demonstrating the evolution of pore formation in the horizontal plane (in set 3) in four typical moments, which were sintering:

(i) the bottom layer/surface of the sample (Fig. 16a),
(ii) mid-layers of the sample, i.e. half-way through the build (Fig. 16b and c),
(iii) layers close to the top surface of the sample (Fig. 16d),
(iv) the top layer/surface (Fig. 16e).

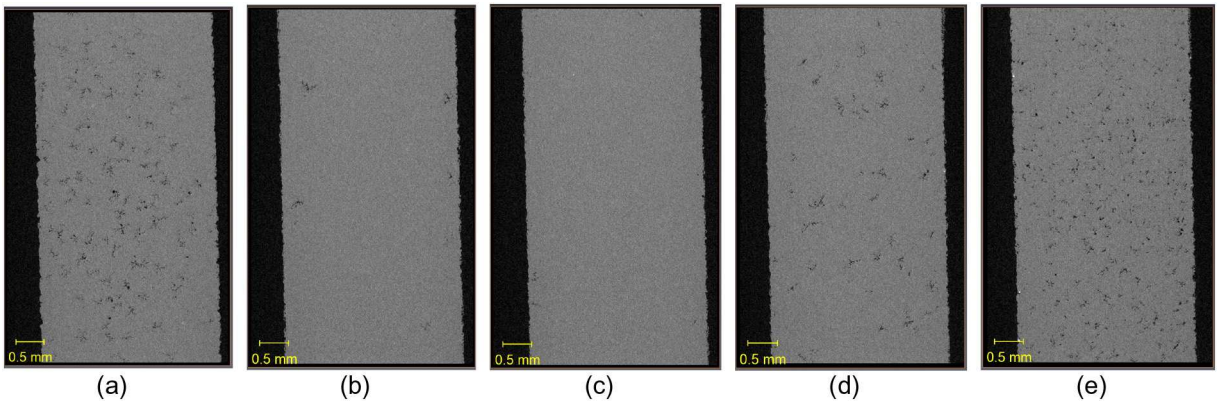

Fig. 16. Pore distribution in the horizontal plane for the sample in set 3 (lamp speed 90 mm/s, energy input 0.037 J/mm^2). (a): bottom layer of the sample; (b) and (c): mid-layers of the sample; (d): a layer close to the top layer/surface; and (e): the top layer/surface of the sample. (Note that the grey is the specimen, the black areas within the specimen are pores and the black areas outside the specimen are the air).

Prior to sintering the bottom layer (i.e. the first layer of the build), there were ten blank layers beneath it which were pre-heated to 160 °C by the heated powder bed. When sintering the bottom layer, there was a temperature difference between the bottom layer and the unsintered layers beneath it. The heat thus tended to dissipate into the un-sintered layers, causing pores to start to form across the bottom layer (Fig. 16a and Fig. 9a). As the HSS build continued, heat continued to accumulate within the sample due to the cyclic thermal dissipation, leading to a higher degree of fusion. As a result, the level of porosity significantly reduced, particularly in the inner area of each layer (please see Fig. 16b and c).

Furthermore, Fig. 16b and c show the distribution of pores in the mid-layers, demonstrating that the presence of pores was mostly in the regions close to the side surfaces where the thermal energy density was most likely to be lower than that in the inner area. This was again largely due to the side surfaces being in contact with the un-sintered surrounding powders and the heat dissipating outwards. As the build progressed towards finishing, the porosity level started to rise again with pores distributing across the whole top layer (Fig. 16d and e), as no further layers were sintered above to provide further heat. The HSS process then underwent a cooling process and thus more pores formed on the top layer. This essentially indicates that thermal energy is a determining factor for pore formation.

4.1.3. Inter-layer and cross-layer pores

As discussed in Sections 4.1.1 and 4.1.2 above, if the energy involved in sintering a layer is below a critical level, there will be a lack of fusion of powder particles and thus pores will be most likely to form on this layer. In addition, when a new layer of powder, which is generally colder than the sintered layer below, is coated, it is likely to result in pores being more inclined to form and lie in between the two layers, developing into inter-layer pores. The pore formation becomes more prominent when there is no sufficient energy that penetrates the current layer to the previous layers. With a further increase in lamp speed, the amount of energy input continued to decrease, eventually leading to a significant lack of fusion between particles (e.g. sets 5 and 6). As a result, pores became increasingly larger (see Fig. 6), some of which further 'propagated' into neighbouring layers, forming cross-layer pores, as shown in Fig. 11b and Fig. 17. Furthermore, it is worth mentioning that powder packing density during powder spreading may also affect porosity of printed parts [52]. This may be influenced by powder physical properties (e.g. particle shape and size [53]) and rheological characteristics (e.g. flowability [54]) as well as other factors (e.g. layer thickness, blade clearance and speed [55]).

4.2. Influence of energy input and pore morphology on mechanical properties

4.2.1. Relation of energy input to mechanical properties

A strong correlation between energy input, porosity and mechanical properties was demonstrated in Fig. 4. With a gradual increase in energy input, the porosity level reduced, thus resulting in a noticeable increase in UTS, EAB and Young's modulus. This suggests that sufficient energy input enables powder particles to fuse and consolidate completely (as shown in Fig. 14a and discussed in Section 4.1.1), undergoing from liquid phase sintering and/or partial melting to full melting in some circumstances [56]. This enhances the mechanical properties to withstand deformation under tensile stress.

The UTS, EAB and Young's modulus of porous tensile bars such as sets 4–6 were found to be significantly lower, as shown in Fig. 4. This was partially because (i) there was less amount of strongly consolidated material (see Fig. 11b) to bear the applied load, (ii) parts that were of high porosity increased chance of crack initiation and propagation due to the large number of inclusions within the part resulting from unfused powder particles [57], (iii) reduced bonding strength (indicated by the clear definition of layers in Fig. 11b) led to the parts being prone to deformation, and (iv) specific pore morphologies (see Section 4.2.2 below). In addition to the above mentioned reasons, it is also worth noting that mechanical properties cannot only be attributed to porosity, and there are other factors that contribute to mechanical properties such as material properties [46] and inter-spherulite interfaces [58]. Having said that, this study has shown that porosity has had a clear influence on mechanical properties of HSS parts. Although porosity and mechanical properties can benefit from a higher energy input, it should be noted that using a high energy input could potentially affect future use of unsintered powder (recycled powder) as it becomes bulked and over-aged.

4.2.2. Influence of pore morphology on mechanical properties

Pore morphology is considered to have an impact on mechanical properties to a certain extent. A typical example is the presence of inter-layer pores, which leads to the part exhibiting anisotropic properties. Delamination is more likely to occur if the load is applied along the build direction, compared with being perpendicularly applied to the build direction. The existence of cross-layer pores is likely to further diminish the mechanical strength.

Pore volume/size may also affect mechanical properties, and larger pores seem to carry a stronger impact. This is deduced from Fig. 4 and Fig. 6 where a higher level of overall porosity led to a larger average pore volume and reduced UTS and EAB. This is also in line with the findings reported in other studies on mechanical properties of laser sintered PA12 parts [17,18]. A high concentration of pores can also contribute to

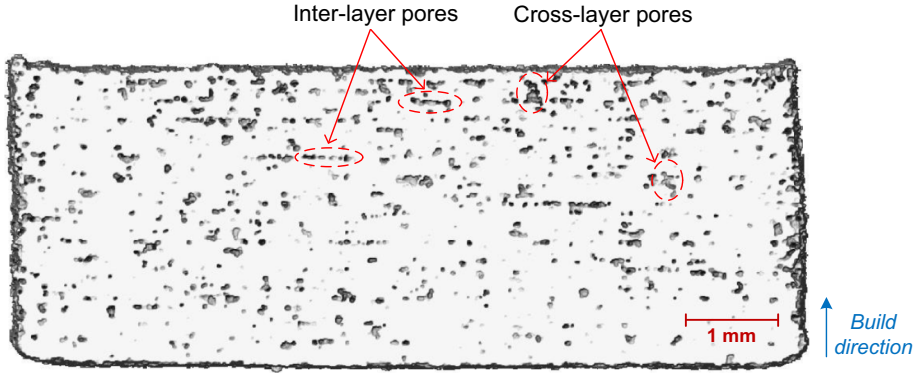

Fig. 17. Volume rendering of the cross-section of inter- and cross-layer pores in set 6, from XCT tomography data.

weakened mechanical properties [12]. However, pore number density is not adequate, as an independent factor, to indicate the possible mechanical properties, as evidenced in Fig. 7. Pores in set 5 outnumbered set 6, but pores in set 6 were larger and interconnected (e.g. large cross-layer pores, as shown in Fig. 17), resulting in a lower number of pores but larger volume. Pore number density represents the number of pores per cubic millimetre within the bulk, irrespective of pore volume/size. Therefore, it should be used together with average pore volume or porosity (volume fraction). This directly contradicts suggestions in the literature [12] that pore number density is the best indicator for mechanical properties, at least in this case. The mechanical properties of the sample is affected not only by the porosity level but also, and more importantly, by the pore size and spatial distribution. A higher population of large pores that reside in surface and sub-surface of the part is more likely to have a greater impact on crack initiation than those pores that are evenly spread across the entire part.

In addition, larger pores tend to be of a lower sphericity (Fig. 13) and they are generally caused by insufficient energy input, thus contributing more to the reduced UTS, EAB and Young's modulus. Therefore, less spherical pores, to a large extent, are considered to be more detrimental to mechanical properties. Given that the shape of less spherical pores usually consists of sharp edges, they are more prone to causing stress concentration while the part is subject to loading. However, in order to precisely determine the influence of the pore morphology on mechanical properties, in-situ XCT scans will be needed to scan the entire gauge length of the tensile bar under tension until the fracture occurs. This will enable local regions of high strain with a particular pore distribution and morphology to be correlated with the final location of failure of the sample.

4.2.3. Comparison of porosity and mechanical properties of parts produced by HSS and MJF

Given that the HSS and HP's commercial MJF techniques share a great deal of similarities, the results obtained in this study were compared with PA12 parts produced by MJF in the literature. However, an unbiased comparison has not been possible at this stage. This is due to MJF process parameters not being fully documented in the literature resulting in large variations of porosity and mechanical properties reported.

For example, O'Connor et al. [33] reported a porosity of 3.2% for MJF PA12 parts, achieving 47 MPa UTS, 19% EAB and 1242 MPa Young's modulus. However, fundamental process parameters used e.g. lamp power and lamp speed were not reported. Moreover, the results were conflicting with their later study where the porosity was found to be less than 1%, but the same UTS, EAB and Young's modules were obtained [19]. Pore distribution was not found to follow any patterns i.e. pores were randomly distributed within the sample. However, by contrast, this study has demonstrated a clear pattern of pore distribution along the build direction at varying energy input levels (as shown in Figs. 8, 9 and 16). It is also noted that the samples in the study by O'Conner et al. [19,33] were densely packed and the printing took 7.5 h to complete in addition to cooling, whereas it was a 1.5 h build in our study. The prolonged build time with densely packed samples would certainly affect the thermal history which could lead to variations in porosity and mechanical properties.

In general, the porosity reported in the literature ranges from less than 1% to 7% (median value ~2%), UTS ranges from 40.1 to 49.9 MPa (median value ~46 MPa), EAB ranges from 2.97% to 27% (median value ~16%), Young's modulus ranges from 1128 MPa to 3938 MPa (median value ~1400 MPa) [19,20,33,59–62]. By comparing the best results obtained by using the lamp speed of 70 mm/s (energy input 0.048 J/mm^2) in this study, it seems that PA12 HSS parts possess a lower porosity (0.14%), slightly lower UTS (44.4 MPa) and EAB (13.5%) but a higher Young's modulus (1793 MPa). However, this comparison result must be used with caution. As mentioned above, certain process parameters used to implement the MJF builds were missing. In addition, the difference in material properties of the commercialised HP 3D High Reusability PA12 [63] and EOS PA12 powders, and the use of mixed virgin and recycled powders in some studies [19,60,61] further introduced additional complications on porosity and mechanical properties of the printed parts.

In order to better understand the difference between HSS- and MJF-processed parts as well as the energy input on the resulting porosity and mechanical properties, crystallinity and degree of particle melt (DPM) will need to be measured. Crystallinity is a result of different applied temperatures and cooling rates [46,64]. Generally, if much of a particle remains unmelted during the sintering process, much of this crystalline character will be retained and thus, crystallinity will be high. A higher crystallinity usually leads to a brittle part in LS [59,65,66]. Previous research in the authors' group [6] revealed the relationship between crystallinity and DFM for the HSS-processed parts, which was that, as the crystallinity decreased, DPM increased, and as a result, EAB improved. However, UTS and Young's modulus did not follow this linear relationship. Therefore, an important step in the future work is to establish the relationship between crystallinity, DPM and porosity, which will help gain a better understanding of how energy input affects mechanical properties.

5. Conclusions

Porosity is generally considered to be undesirable defects that are detrimental to mechanical properties of AM parts. High Speed Sintering is a novel PBF polymer AM technique, which is different to other polymer AM processes (e.g. Laser Sintering) in terms of thermal behaviour. However, there is a lack of understanding of porosity of parts produced via HSS. Therefore, this study investigated the influence of thermal energy input on the porosity and mechanical properties of HSS PA12 parts. Pore volume fraction, size, shape, number density and spatial distribution were systematically examined using the XCT technique.

Porosity and mechanical properties were found to be closely correlated, which was linked with energy input. A greater amount of energy input can significantly reduce the level of porosity, resulting in improved mechanical properties. The lowest porosity found in this study was 0.14%, which led to 44.4 MPa, 13.5% and 1796 MPa in UTS, EAB and Young's modulus, respectively. The highest porosity measured was 7.36%, which resulted from the lowest amount of energy input (0.028 J/mm^2). This led to a significant decrease in mechanical properties with the UTS of 28.6 MPa, EAB of 4.2% and Young's modulus of 1052 MPa. Porosity level is a superior indicator for mechanical properties and typically, a higher level indicates a lower UTS, EAB and Young's modulus. An increase in porosity also indicates an increased average pore size but not necessarily a higher pore number density. Larger pores tend to be in a more irregular shape that is of a low sphericity, and are likely to have a greater but negative impact on mechanical properties.

It was revealed that thermal energy input is the fundamental reason causing pores to form. The amount of energy input largely determines the degree of fusion between powder particles. Incomplete fusion does not allow molten polymer to form necks and completely consolidate, creating spaces between adjacent particles within a layer and/or between layers, resulting in pore formation. On the other hand, unlike other PBF AM processes such as LS and SLM where overly high energy input may negatively affect porosity and mechanical properties, this study showed that HSS generally benefited from a high level of energy input. In addition, the spatial distribution of pores were examined. The vast majority of pores in the samples of low porosity levels (sets 1 to 3) was found to be located in areas close to top, bottom and side surfaces which were the boundaries in contact with surrounding unsintered powders. The presence of inter- and cross-layer pores was largely found in the samples of high porosity levels (e.g. sets 4 to 6), indicating a significant lack of energy input within layers. Future work will focus on exploring the influence of energy input on the sintering process in

terms of degree of particle melt and crystallinity. Efforts will also be made to understand the effect of sub-surface pores in terms of morphology and distribution on crack initiation and associated impacts on mechanical properties.

Data availability

Representative samples of the research data are given in the figures and tables. Other datasets generated and/or analysed during this study are not publicly available due to their large size but are available from the corresponding author upon reasonable request.

Declaration of Competing Interest

The authors declare that they have no known competing financial interests or personal relationships that could have appeared to influence the work reported in this paper.

Acknowledgements

This work was supported by the UK Engineering and Physical Sciences Research Council, grant number EP/P006566/1. Technical support from the Henry Moseley X-ray Imaging Facility at the University of Manchester is also appreciated. Thanks also go to Dr. Julia Behnsen at Manchester University for her assistance in XCT scanning and data analysis, and Mr. Kurt Bonser and Mr. Christopher Hill at Sheffield University for their assistance in HSS processing and SEM imaging, respectively.

References

[1] T.D. Ngo, A. Kashani, G. Imbalzano, K.T.Q. Nguyen, D. Hui, Additive manufacturing (3D printing): a review of materials, methods, applications and challenges, Compos. Part B 143 (2018) 172–196, https://doi.org/10.1016/j.compositesb.2018.02.012.
[2] S. Liu, Y.C. Shin, Additive manufacturing of Ti6Al4V alloy: a review, Mater. Des. 164 (2019) 107552, https://doi.org/10.1016/j.matdes.2018.107552.
[3] S.A.M. Tofail, E.P. Koumoulos, A. Bandyopadhyay, S. Bose, L. O'Donoghue, C. Charitidis, Additive manufacturing: scientific and technological challenges, market uptake and opportunities, Mater. Today 21 (2018) 22–37, https://doi.org/10.1016/j.mattod.2017.07.001.
[4] M. Schmidt, M. Merklein, D. Bourell, D. Dimitrov, T. Hausotte, K. Wegener, L. Overmeyer, F. Vollertsen, G.N. Levy, Laser based additive manufacturing in industry and academia, CIRP Ann. 66 (2017) 561–583, https://doi.org/10.1016/j.cirp.2017.05.011.
[5] Y. Kok, X.P. Tan, P. Wang, M.L.S. Nai, N.H. Loh, E. Liu, S.B. Tor, Anisotropy and heterogeneity of microstructure and mechanical properties in metal additive manufacturing: a critical review, Mater. Des. 139 (2018) 565–586, https://doi.org/10.1016/j.matdes.2017.11.021.
[6] A. Ellis, C.J. Noble, N. Hopkinson, High speed sintering: assessing the influence of print density on microstructure and mechanical properties of nylon parts, Addit. Manuf. 1 (2014) 48–51, https://doi.org/10.1016/j.addma.2014.07.003.
[7] A. Thompson, I. Maskery, R.K. Leach, X-ray computed tomography for additive manufacturing: a review, Meas. Sci. Technol. 27 (2016) 072001.
[8] C. Panwisawas, C.L. Qiu, Y. Sovani, J.W. Brooks, M.M. Attallah, H.C. Basoalto, On the role of thermal fluid dynamics into the evolution of porosity during selective laser melting, Scr. Mater. 105 (2015) 14–17, https://doi.org/10.1016/j.scriptamat.2015.04.016.
[9] A. Du Plessis, I. Yadroitsev, I. Yadroitsava, S.G. Le Roux, X-ray microcomputed tomography in additive manufacturing: a review of the current technology and applications, 3D Printing and Additive Manufacturing, 5, 2018, pp. 227–247.
[10] D. Rouholamin, N. Hopkinson, Understanding the efficacy of micro-CT to analyse high speed sintering parts, Rapid Prototyp. J. 22 (2016) 152–161.
[11] W. Dewulf, M. Pavan, T. Craeghs, J.-P. Kruth, Using X-ray computed tomography to improve the porosity level of polyamide-12 laser sintered parts, CIRP Ann. 65 (2016) 205–208.
[12] T. Stichel, T. Frick, T. Laumer, F. Tenner, T. Hausotte, M. Merklein, M. Schmidt, A round Robin study for selective laser sintering of polymers: Back tracing of the pore morphology to the process parameters, J. Mater. Process. Technol. 252 (2018) 537–545, https://doi.org/10.1016/j.jmatprotec.2017.10.013.
[13] D.I. Stoia, L. Marşavina, E. Linul, Correlations between process parameters and outcome properties of laser-sintered polyamide, Polymers 11 (2019) 1850, https://doi.org/10.3390/polym11111850.
[14] A. Liebrich, H.C. Langowski, R. Schreiber, B.R. Pinzer, Porosity distribution in laser-sintered polymeric thin sheets as revealed by X-ray micro tomography, Polym. Test. 76 (2019) 286–297, https://doi.org/10.1016/j.polymertesting.2019.02.014.
[15] I. Flores Ituarte, O. Wiikinkoski, A. Jansson, Additive manufacturing of polypropylene: a screening design of experiment using laser-based powder bed fusion, Polymers 10 (2018) 1293, https://doi.org/10.3390/polym10121293.
[16] M. Pavan, T. Craeghs, R. Verhelst, O. Ducatteeuw, J.-P. Kruth, W. Dewulf, CT-based quality control of laser sintering of polymers, Case Studies in Nondestructive Testing and Evaluation, 6, 2016, pp. 62–68, https://doi.org/10.1016/j.csndt.2016.04.004.
[17] M. Pavan, M. Faes, D. Strobbe, B. Van Hooreweder, T. Craeghs, D. Moens, W. Dewulf, On the influence of inter-layer time and energy density on selected critical-to-quality properties of PA12 parts produced via laser sintering, Polym. Test. 61 (2017) 386–395, https://doi.org/10.1016/j.polymertesting.2017.05.027.
[18] S. Dupin, O. Lame, C. Barrès, J.-Y. Charmeau, Microstructural origin of physical and mechanical properties of polyamide 12 processed by laser sintering, Eur. Polym. J. 48 (2012) 1611–1621, https://doi.org/10.1016/j.eurpolymj.2012.06.007.
[19] H.J. O' Connor, D.P., Dowling, comparison between the properties of polyamide 12 and glass bead filled polyamide 12 using the multi jet fusion printing process, Addit. Manuf. 31 (2020) 100961, https://doi.org/10.1016/j.addma.2019.100961.
[20] G. Craft, J. Nussbaum, N. Crane, J.P. Harmon, Impact of extended sintering times on mechanical properties in PA-12 parts produced by powderbed fusion processes, Addit. Manuf. 22 (2018) 800–806, https://doi.org/10.1016/j.addma.2018.06.028.
[21] M. Åsberg, G. Fredriksson, S. Hatami, W. Fredriksson, P. Krakhmalev, Influence of post treatment on microstructure, porosity and mechanical properties of additive manufactured H13 tool steel, Mater. Sci. Eng. A 742 (2019) 584–589, https://doi.org/10.1016/j.msea.2018.08.046.
[22] S. Tammas-Williams, P.J. Withers, I. Todd, P.B. Prangnell, Porosity regrowth during heat treatment of hot isostatically pressed additively manufactured titanium components, Scr. Mater. 122 (2016) 72–76, https://doi.org/10.1016/j.scriptamat.2016.05.002.
[23] P. Kumar, J. Farah, J. Akram, C. Teng, J. Ginn, M. Misra, Influence of laser processing parameters on porosity in Inconel 718 during additive manufacturing, Int. J. Adv. Manuf. Technol. 103 (2019) 1497–1507, https://doi.org/10.1007/s00170-019-03655-9.
[24] Z.E.E. Tan, J.H.L. Pang, J. Kaminski, H. Pepin, Characterisation of porosity, density, and microstructure of directed energy deposited stainless steel AISI 316L, Addit. Manuf. 25 (2019) 286–296, https://doi.org/10.1016/j.addma.2018.11.014.
[25] X. Wang, L. Zhao, J.Y.H. Fuh, H.P. Lee, Effect of porosity on mechanical properties of 3D printed polymers: experiments and micromechanical modeling based on X-ray computed tomography analysis, Polymers 11 (2019) 1154, https://doi.org/10.3390/polym11071154.
[26] A.A. Martin, N.P. Calta, S.A. Khairallah, J. Wang, P.J. Depond, A.Y. Fong, V. Thampy, G.M. Guss, A.M. Kiss, K.H. Stone, C.J. Tassone, J. Nelson Weker, M.F. Toney, T. van Buuren, M.J. Matthews, Dynamics of pore formation during laser powder bed fusion additive manufacturing, Nat. Commun. 10 (2019) 1987, https://doi.org/10.1038/s41467-019-10009-2.
[27] H.D. Carlton, A. Haboub, G.F. Gallegos, D.Y. Parkinson, A.A. MacDowell, Damage evolution and failure mechanisms in additively manufactured stainless steel, Mater. Sci. Eng. A 651 (2016) 406–414, https://doi.org/10.1016/j.msea.2015.10.073.
[28] I. Maskery, N.T. Aboulkhair, M.R. Corfield, C. Tuck, A.T. Clare, R.K. Leach, R.D. Wildman, I.A. Ashcroft, R.J.M. Hague, Quantification and characterisation of porosity in selectively laser melted Al–Si10–Mg using X-ray computed tomography, Mater. Charact. 111 (2016) 193–204, https://doi.org/10.1016/j.matchar.2015.12.001.
[29] S. Siddique, M. Imran, M. Rauer, M. Kaloudis, E. Wycisk, C. Emmelmann, F. Walther, Computed tomography for characterization of fatigue performance of selective laser melted parts, Mater. Des. 83 (2015) 661–669, https://doi.org/10.1016/j.matdes.2015.06.063.
[30] S. Tammas-Williams, H. Zhao, F. Léonard, F. Derguti, I. Todd, P.B. Prangnell, XCT analysis of the influence of melt strategies on defect population in Ti–6Al–4V components manufactured by selective Electron beam melting, Mater. Charact. 102 (2015) 47–61, https://doi.org/10.1016/j.matchar.2015.02.008.
[31] A.R. Zekavat, A. Jansson, J. Larsson, L. Pejryd, Investigating the effect of fabrication temperature on mechanical properties of fused deposition modeling parts using X-ray computed tomography, Int. J. Adv. Manuf. Technol. 100 (2019) 287–296, https://doi.org/10.1007/s00170-018-2664-8.
[32] C.E. Majewski, D. Oduye, H.R. Thomas, N. Hopkinson, Effect of infra-red power level on the sintering behaviour in the high speed sintering process, Rapid Prototyp. J. 14 (2008) 155–160, https://doi.org/10.1108/13552540810878012.
[33] H.J. O'Connor, A.N. Dickson, D.P. Dowling, Evaluation of the mechanical performance of polymer parts fabricated using a production scale multi jet fusion printing process, Addit. Manuf. 22 (2018) 381–387, https://doi.org/10.1016/j.addma.2018.05.035.
[34] J. Liu, Y. Song, C. Chen, X. Wang, H. Li, C.A. Zhou, J. Wang, K. Guo, J. Sun, Effect of scanning speed on the microstructure and mechanical behavior of 316L stainless steel fabricated by selective laser melting, Mater. Des. 186 (2020) 108355, https://doi.org/10.1016/j.matdes.2019.108355.
[35] M. Ghayoor, K. Lee, Y. He, C.-h. Chang, B.K. Paul, S. Pasebani, Selective laser melting of 304L stainless steel: role of volumetric energy density on the microstructure, texture and mechanical properties, Addit. Manuf. 32 (2020) 1–13, https://doi.org/10.1016/j.addma.2019.101011.
[36] Victory-Lighting, Integrated reflectors2018 , available at https://www.victorylighting.co.uk/site/wp-content/uploads/2018/08/Reflector-coated-lamps-v1.2-EN.pdf accessed on 10/6/2020.
[37] ASTM, D638-02a: Standard Test Method for Tensile Properties of Plastics, 2017.
[38] M. Ritchie, Print quality requirements for single-pass inkjet printing – the whole picture, Xaar 3D Ltd., 2017 , avaialble at https://www.xaar.com/en/resource-centre/print-quality-the-whole-picture/ accessed on 21/5/2020.
[39] N. Otsu, A threshold selection method from gray-level histograms, IEEE Transactions on Systems, Man, and Cybernetics, 9, 1979, pp. 62–66.

[40] C.T. Bellehumeur, M. Kontopoulou, J. Vlachopoulos, The role of viscoelasticity in polymer sintering, Rheol. Acta 37 (1998) 270–278, https://doi.org/10.1007/s003970050114.
[41] L. Benedetti, B. Brulé, N. Decraemer, K.E. Evans, O. Ghita, Evaluation of particle coalescence and its implications in laser sintering, Powder Technol. 342 (2019) 917–928, https://doi.org/10.1016/j.powtec.2018.10.053.
[42] F. Wakai, K. Katsura, S. Kanchika, Y. Shinoda, T. Akatsu, K. Shinagawa, Sintering force behind the viscous sintering of two particles, Acta Mater. 109 (2016) 292–299, https://doi.org/10.1016/j.actamat.2016.03.006.
[43] J. Frenkel, Viscous flow of crystalline bodies under the action of surface tension, J. Phys. 9 (1945) 385.
[44] J. Eshelby, Discussion of paper by AJ Shaler, seminar on the kinetics of sintering, Trans. AIME 185 (1949) 806.
[45] A.J. Shaler, Seminar on the kinetics of sintering, JOM 1 (1949) 796–813, https://doi.org/10.1007/BF03398399.
[46] R.D. Goodridge, C.J. Tuck, R.J.M. Hague, Laser sintering of polyamides and other polymers, Prog. Mater. Sci. 57 (2012) 229–267, https://doi.org/10.1016/j.pmatsci.2011.04.001.
[47] J. Bai, B. Zhang, J. Song, G. Bi, P. Wang, J. Wei, The effect of processing conditions on the mechanical properties of polyethylene produced by selective laser sintering, Polym. Test. 52 (2016) 89–93, https://doi.org/10.1016/j.polymertesting.2016.04.004.
[48] M. Schmid, A. Amado, K. Wegener, Materials perspective of polymers for additive manufacturing with selective laser sintering, J. Mater. Res. 29 (2014) 1824–1832, https://doi.org/10.1557/jmr.2014.138.
[49] I.-G. Lee, D.-H. Kim, K.-H. Jung, H.-J. Kim, H.-S. Kim, Effect of the cooling rate on the mechanical properties of glass fiber reinforced thermoplastic composites, Compos. Struct. 177 (2017) 28–37, https://doi.org/10.1016/j.compstruct.2017.06.007.
[50] P. Wang, W.J. Sin, M.L.S. Nai, J. Wei, Effects of processing parameters on surface roughness of additive manufactured Ti-6Al-4V via Electron beam melting, Materials 10 (2017) 1121, https://doi.org/10.3390/ma10101121.
[51] S.R. Athreya, K. Kalaitzidou, S. Das, Processing and characterization of a carbon black-filled electrically conductive Nylon-12 nanocomposite produced by selective laser sintering, Mater. Sci. Eng. A 527 (2010) 2637–2642, https://doi.org/10.1016/j.msea.2009.12.028.
[52] U. Ali, Y. Mahmoodkhani, S. Imani Shahabad, R. Esmaeilizadeh, F. Liravi, E. Sheydaeian, K.Y. Huang, E. Marzbanrad, M. Vlasea, E. Toyserkani, On the measurement of relative powder-bed compaction density in powder-bed additive manufacturing processes, Mater. Des. 155 (2018) 495–501, https://doi.org/10.1016/j.matdes.2018.06.030.
[53] C. Meier, R. Weissbach, J. Weinberg, W.A. Wall, A.J. Hart, Critical influences of particle size and adhesion on the powder layer uniformity in metal additive manufacturing, J. Mater. Process. Technol. 266 (2019) 484–501, https://doi.org/10.1016/j.jmatprotec.2018.10.037.
[54] S.E. Brika, M. Letenneur, C.A. Dion, V. Brailovski, Influence of particle morphology and size distribution on the powder flowability and laser powder bed fusion manufacturability of Ti-6Al-4V alloy, Addit. Manuf. 31 (2020) 100929, https://doi.org/10.1016/j.addma.2019.100929.
[55] S. Haeri, Optimisation of blade type spreaders for powder bed preparation in additive manufacturing using DEM simulations, Powder Technol. 321 (2017) 94–104, https://doi.org/10.1016/j.powtec.2017.08.011.
[56] J.P. Kruth, P. Mercelis, J. Van Vaerenbergh, L. Froyen, M. Rombouts, Binding mechanisms in selective laser sintering and selective laser melting, Rapid Prototyp. J. 11 (2005) 26–36, https://doi.org/10.1108/13552540510573365.
[57] B. Van Hooreweder, F. De Coninck, D. Moens, R. Boonen, P. Sas, Microstructural characterization of SLS-PA12 specimens under dynamic tension/compression excitation, Polym. Test. 29 (2010) 319–326, https://doi.org/10.1016/j.polymertesting.2009.12.006.
[58] H. Zarringhalam, N. Hopkinson, N.F. Kamperman, J.J. de Vlieger, Effects of processing on microstructure and properties of SLS nylon 12, Mater. Sci. Eng. A 435-436 (2006) 172–180, https://doi.org/10.1016/j.msea.2006.07.084.
[59] Z. Xu, Y. Wang, D. Wu, K.P. Ananth, J. Bai, The process and performance comparison of polyamide 12 manufactured by multi jet fusion and selective laser sintering, J. Manuf. Process. 47 (2019) 419–426, https://doi.org/10.1016/j.jmapro.2019.07.014.
[60] D. Tasch, M. Schagerl, B. Wazel, G. Wallner, Impact behavior and fractography of additively manufactured polymers: laser sintering, multijet fusion, and hot lithography, Addit. Manuf. 29 (2019) 100816, https://doi.org/10.1016/j.addma.2019.100816.
[61] F. Sillani, R.G. Kleijnen, M. Vetterli, M. Schmid, K. Wegener, Selective laser sintering and multi jet fusion: process-induced modification of the raw materials and analyses of parts performance, Addit. Manuf. 27 (2019) 32–41, https://doi.org/10.1016/j.addma.2019.02.004.
[62] S. Morales-Planas, J. Minguella-Canela, J. Lluma-Fuentes, J.A. Travieso-Rodriguez, A.-A. García-Granada, Multi jet fusion PA12 manufacturing parameters for Watertightness, strength and tolerances, Materials 11 (2018) 1472, https://doi.org/10.3390/ma11081472.
[63] H.P. Hewlett-Packard, Multi Jet Fusion Technology, avaialble at www8.hp.com/uk/en/printers/3d-printers/products/multi-jet-technology.html 2020.
[64] H. Zarringhalam, Investigation into crystallinity and degree of particle melt in selective laser sintering, PhD thesis, Loughborough University, UK, 2007.
[65] S. Griessbach, R. Lach, W. Grellmann, Structure–property correlations of laser sintered nylon 12 for dynamic dye testing of plastic parts, Polym. Test. 29 (2010) 1026–1030, https://doi.org/10.1016/j.polymertesting.2010.09.010.
[66] D. Drummer, D. Rietzel, F. Kühnlein, Development of a characterization approach for the sintering behavior of new thermoplastics for selective laser sintering, Phys. Procedia 5 (2010) 533–542, https://doi.org/10.1016/j.phpro.2010.08.081.